

What Limits the Rate Capability of Ultrathick Composite Electrodes in Lithium-Ion Batteries? A Case Study on the Thickness-Dependent Impedance of LiCoO₂ Cathodes

Marvin Cronau,^[a] Alexander Paulus,^[a] Lars Pateras Pescara,^[a] Moritz Kroll,^[a] Diemo Renz,^[a] Joëlle Aurelie Mekontso,^[a] Anna Marx,^[a] and Bernhard Roling^{*[a]}

Increasing the thickness of composite electrodes in lithium-ion batteries from about 80–100 µm in state-of-the-art commercial cells to several 100 µm would enhance the energy density, however at the expense of the power density. Despite this common knowledge, quantitative studies on the impedance and rate capability of composite electrode in dependence of the electrode thickness are scarce. Therefore, we have carried out a case study on LiCoO₂ composite electrodes with thicknesses up to about 250 µm. We first demonstrate that

conventional composite electrode preparation leads to ion transport tortuosities in the electrolyte-filled pores, which are virtually independent of the thickness. The thickness-dependent impedance of these electrodes decreases with increasing thickness and follows the predictions of a generalized transmission line (GTL) model. We use the GTLM model for analyzing in what way cycling of ultrathick electrodes (250–300 µm) with a rate of 1 C should be achievable.

Introduction

The growing awareness of climate change leads to an enhanced demand for ecofriendly power supply and, along with this, improved storage capabilities. Lithium-ion batteries (LIB) are one of the most promising candidates for the application in mobile devices, as they offer a high volumetric and gravimetric energy density. Especially for the application in electric vehicles, the energy density has to be increased.^[1] In the recent past, the energy density of commercial cells has already been significantly increased by using new cathode materials based on lithium nickel manganese cobalt oxide (NMC) and on lithium nickel cobalt aluminum oxides (NCA),^[2–7] as well as by adding a small amount of silicon to the anode.^[8–11] Alternative approaches are a reduction of the amount of inactive materials (storing no energy) like binder and conductive additives,^[12] the targeted structuring of the pore space in order to reduce the ion transport tortuosity,^[13–16] and the usage of highly concentrated electrolytes in order to avoid electrolyte depletion close to the active material particles.^[17]

Another approach is the preparation of ultrathick electrodes. This leads also to lower fraction of inactive materials in the cell (separator, current collectors, casing) and thus to a higher energy density. However, as has been shown in several studies,^[18–22] electrodes with thickness in the range of several 100 µm can suffer from poor rate capabilities, which is detrimental for the application in EVs. Gao et al. measured the Li⁺ diffusion coefficient in ultrathick NMC electrodes and reported a drop of the lithium diffusion coefficient by more than two orders of magnitude when increasing the electrode thickness from about 100 µm to about 300 µm.^[23] However, in many of these studies, the morphology of the electrodes in dependence of the thickness was not analyzed. For instance, an electrode preparation process leading to an increasingly inhomogeneous distribution of the active material particles with increasing electrode thickness would most likely lead to higher ion transport tortuosities in ultrathick electrodes and in turn to a lower rate capability.

Here, we report on a case study on the impedance and rate capability of LiCoO₂ electrodes with thicknesses in the range from 44 µm to 251 µm. LiCoO₂ was chosen as reference material for this case study, since its high electronic and ionic conductivity is advantageous for high-rate capabilities. Galvanostatic charge/discharge curves and impedance spectra at 50% state of charge (SOC) of these electrodes were taken and analyzed in the framework of a generalized transmission line model (GTL). We show that the thickness-dependent impedance follows the predictions of the GTLM, so that the GTLM can be used for analyzing the rate capability of ultrathick electrodes in dependence of the size and the electrochemical properties of the active material particles. From these results, we draw conclusions about possible means for enabling fast cycling of ultrathick LCO electrodes. These means should also

[a] Dr. M. Cronau, A. Paulus, L. P. Pescara, Dr. M. Kroll, Dr. D. Renz, J. A. Mekontso, A. Marx, Prof. Dr. B. Roling
Department of Chemistry and Center for Materials Science (WZMW), University of Marburg, Hans-Meerwein-Strasse 4, 35032 Marburg, Germany
E-mail: roling@staff.uni-marburg.de
Homepage: <https://www.uni-marburg.de/de/fb15/arbeitsgruppen/ag-roling>

 Supporting information for this article is available on the WWW under <https://doi.org/10.1002/batt.202200194>

 © 2022 The Authors. *Batteries & Supercaps* published by Wiley-VCH GmbH. This is an open access article under the terms of the Creative Commons Attribution Non-Commercial NoDerivs License, which permits use and distribution in any medium, provided the original work is properly cited, the use is non-commercial and no modifications or adaptations are made.

be relevant for cathodes based on other active materials, such as NMC.

Results and Discussion

In Figure 1(a), we show impedance spectra of symmetric cells (cathode | separator | cathode) for cathodes with different volume fractions of the electrolyte inside the pore space, ε_e . The measurements were performed at 0% state of charge (SOC), i.e., under ion-blocking-conditions. In this case, the impedance $Z_{\text{SOC}0}$ can be described in the framework of a specific transmission line model:^[24–26]

$$Z_{\text{SOC}0} = \sqrt{\frac{R_{\text{ion}}}{Q_{\text{DL}}(j\omega)^\beta}} \coth \left(\sqrt{R_{\text{ion}} Q_{\text{DL}}(j\omega)^\beta} \right) \quad (1)$$

Here, R_{ion} is the ion transport resistance. The non-ideal double layer capacitance of active materials / electrolyte interface is described by a constant-phase element (CPE) with prefactor Q_{DL} and exponent β . j is the imaginary unit and ω the angular frequency. The impedance spectrum is characterized by a slope close to 45° at high frequencies and by a non-ideal double layer capacitance at low frequencies. At low frequencies, $Z_{\text{SOC}0}$ can be approximated by:

$$Z_{\text{SOC}0} = \frac{R_{\text{ion}}}{3} + \frac{1}{Q_{\text{DL}}(j\omega)^\beta} \quad (2)$$

The ion-blocking conditions in this cell setup are based on a very high charge-transfer resistance of the active material in the fully lithiated state, see also Figure S5. As can be seen from Figure 1(a), the ion transport resistance decreases with increasing volume fraction of the electrolyte ε_e . Figure 1(b) shows impedance spectra for an electrolyte volume fraction $\varepsilon_e = 0.32$ and for varying thickness of the electrode. In this case, the ion transport resistance R_{ion} increases with increasing electrode thickness l .

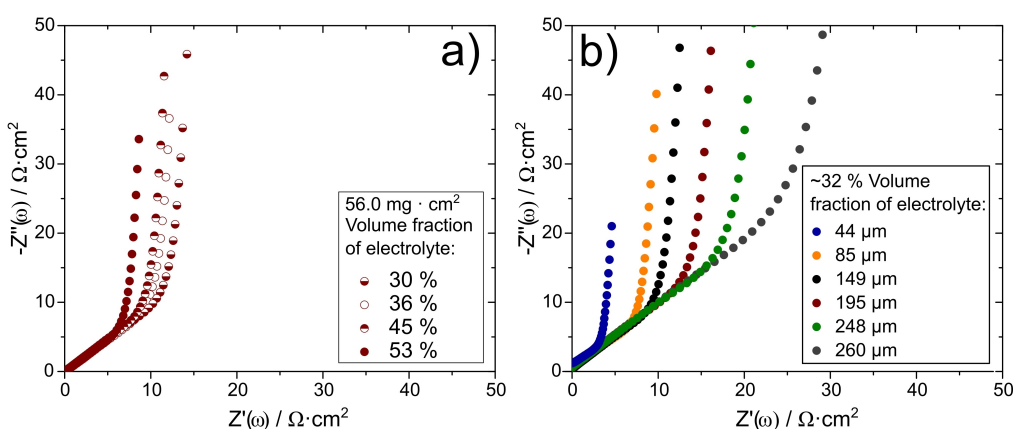


Figure 1. a) Impedance spectra of electrodes with a material loading of 56 mg/cm² and different volume fraction of electrolyte. The resulting electrode thicknesses are in a range of 160–290 µm. b) Impedance spectra of electrodes with 32% volume fraction of the electrolyte and different thicknesses l .

After determining R_{ion} from fits of the spectra to Equation (1), the tortuosity of the ion transport was calculated as:^[24]

$$\tau_{\text{EIS}} = \frac{\sigma_{\text{bulk}} \cdot R_{\text{ion}} \cdot A}{2 l} \cdot \varepsilon_e \quad (3)$$

Here, σ_{bulk} and A denote the bulk ionic conductivity of the electrolyte and the electrode area, respectively. We note that the ion-blocking TLM model used here [Eqs. (1) and (2)] is based on the assumption of cylindrical pores in the electrode and neglects possible agglomerations of active materials particles and the existence of strong pore constrictions and dead-end pores. NGUYEN et al.^[27] showed that the presence of dead end pores leads to a deviation from the 45° slope at high frequencies and to semicircle-like features in the impedance spectra. Such deviations from the 45° slope were also observed in 4D-resolved physical models for NMC-based cathodes.^[28] Since our spectra do not exhibit such non-ideal features, we applied the ion-blocking transmission line model. In principle, τ_{EIS} should be identical to the tortuosity factor $\tau_{\text{simulation}}$ obtained in simulations of ion transport in reconstructed electrodes. However, in several cases, τ_{EIS} was found to be higher than $\tau_{\text{simulation}}$.^[26,29] This discrepancy might be caused by the limited spatial resolution of FIB/SEM-based reconstruction. Due to the limited spatial resolution, transport bottlenecks with sizes below the resolution limit might not be detected, leading to an underestimation of the tortuosity.

In Figure 2(a–e), the ion transport tortuosities τ_{EIS} are plotted versus the electrolyte volume fraction ε_e for electrodes in different thickness ranges. In all ranges, the τ_{EIS} vs. ε_e data can be fitted by a Bruggeman relation $\tau_{\text{EIS}} = A \cdot \varepsilon_e^{-\alpha}$. In Figure 2 f), the Bruggeman fits are compared for different thickness ranges. Overall, there is weak dependence of the ion transport tortuosity on the electrode thickness with a tendency that the tortuosity decreases slightly with increasing thickness. In the case of composite electrodes for commercial lithium-ion batteries, the volume fraction of electrolyte is typically in the range of 30%.^[30] In this range, the determined tortuosities are

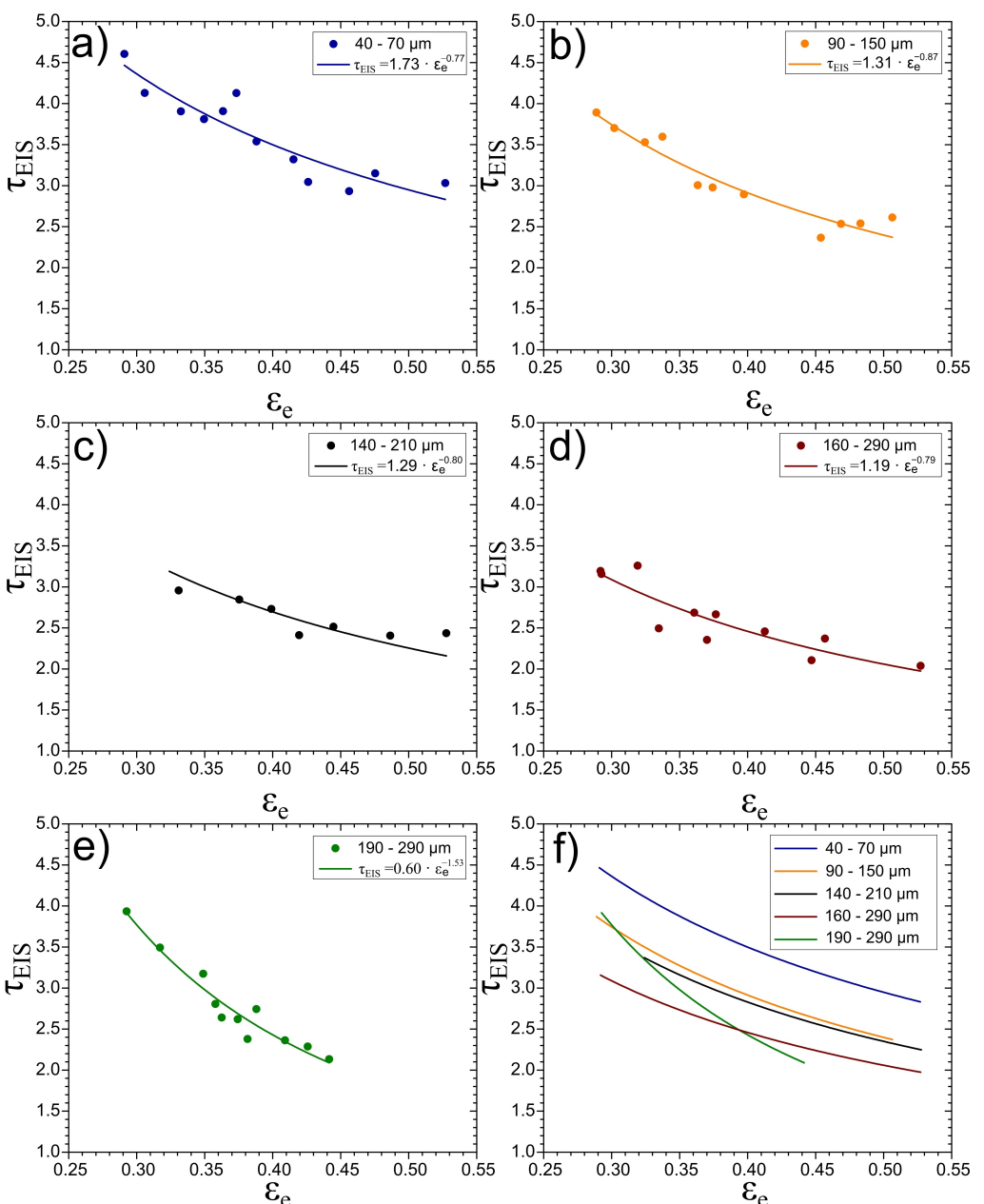


Figure 2. Ion transport tortuosity τ_{EIS} vs. volume fraction of electrolyte ε_e for electrodes in different thickness ranges. a) 40–70 μm , b) 90–150 μm , c) 140–210 μm , d) 160–290 μm , e) 190–290 μm . f) Comparison of fits in (a–e).

between 2.7 and 4.5, in good accordance with values from the literature.^[24–26,29]

Considering the weak thickness dependence of the ion transport tortuosity and the rather ideal shape of the impedance spectra of the symmetric cells in Figure 1, we have no indication for a significant change of the electrode morphology with increasing thickness. In Figure 3, we show exemplary FIB-SEM cross sections of electrodes with 101 μm and with 251 μm thickness, respectively. The images show no significant differences in the distribution of the LiCoO₂ particles inside the composite electrodes and thus give no indication for a thickness-dependent cathode morphology.

In Figure 4 we show galvanostatic charge/discharge curves of cathodes with an electrolyte volume fraction $\varepsilon_e = 0.35$. The curves are plotted for the third cycle at a low rate of 0.1 C. In this case, the overpotentials are low, and all electrodes show a discharge capacity of about 145 mAh/g, which is in good agreement with literature values and values reported for commercial cells.^[31,32] It is noticeable that the overvoltage increases with increasing thickness. In order to estimate the total resistance of the cathodes during cycling, R_{tot} , the difference between the charging and the discharging voltage in an SOC50 state was determined, and the overvoltage was assumed to be 50% of this value. Under this assumption, the total resistance is given by $R_{\text{tot}} = (U_{\text{charge}} - U_{\text{discharge}})/(2 \cdot j)$ with

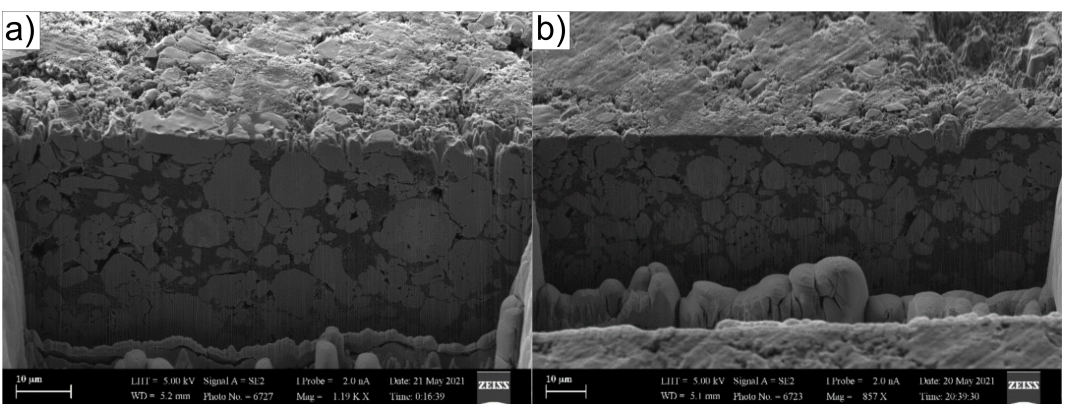


Figure 3. Cross section SEM image of electrode with a thickness of a) 101 μm and b) 251 μm .

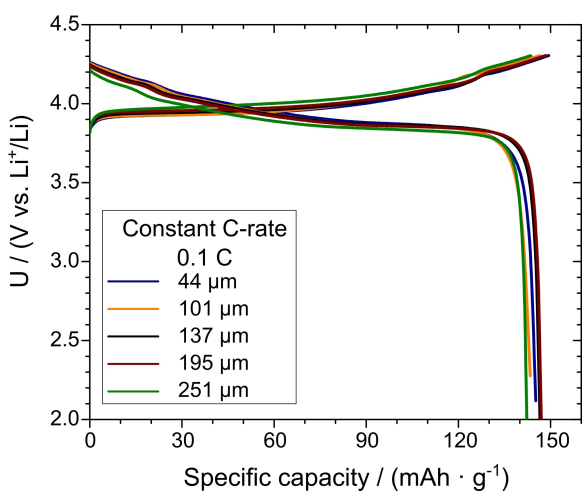


Figure 4. Galvanostatic cycling curves of electrodes with an electrolyte volume fraction of $\varepsilon_e = 0.35$. The cycling experiments were performed at a rate of 0.1 C.

j denoting the current density. The values obtained for R_{tot} are given in Table S1. The total resistance R_{tot} decreases from 194 $\Omega \cdot \text{cm}^2$ for the thinnest electrode (44 μm) to 75 $\Omega \cdot \text{cm}^2$ for the thickest electrode (251 μm).

In order to analyze the impedance of the cathodes in more detail, we carried out impedance measurements on cathodes with an electrolyte volume fraction $\varepsilon_e = 0.35$ at SOC50. The impedance spectra are shown in Figure 5. In these spectra, the high-frequency resistance caused by the electrolyte-filled separator resistance between cathode and reference electrode was subtracted in order to obtain the cathode impedance. The spectra are characterized by a semicircle at high frequencies and a Warburg impedance at low frequencies. Both the diameter of the semicircle and the Warburg impedance decrease with increasing thickness of the cathodes. In order to quantify this, we define two resistances, the resistance of the semicircle $R_{\text{semicircle}}$ and a resistance given by the modulus of the impedance at the lowest frequency of 10^{-4} Hz, $R_{\text{lf}} = |Z(10^{-4}\text{Hz})|$. The values obtained for these resistances are given in Table S1 and are plotted in Figure 6 together with the resistance R_{tot} versus the electrode thickness. The values

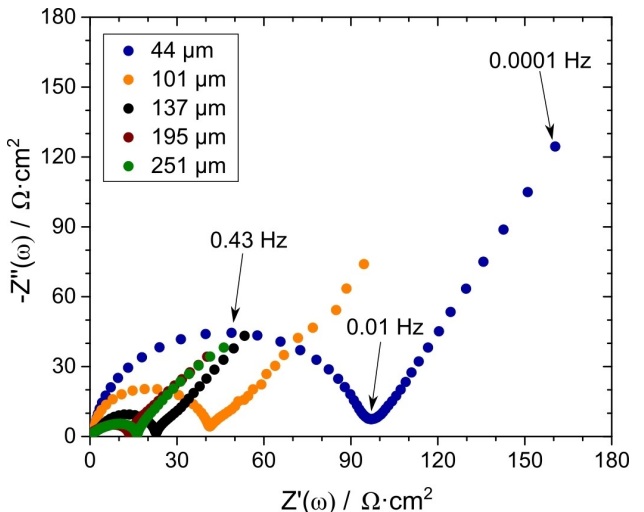


Figure 5. Impedance spectra of cathodes with an electrolyte volume fraction of $\varepsilon_e = 0.35$ at 50% state of charge (SOC50).

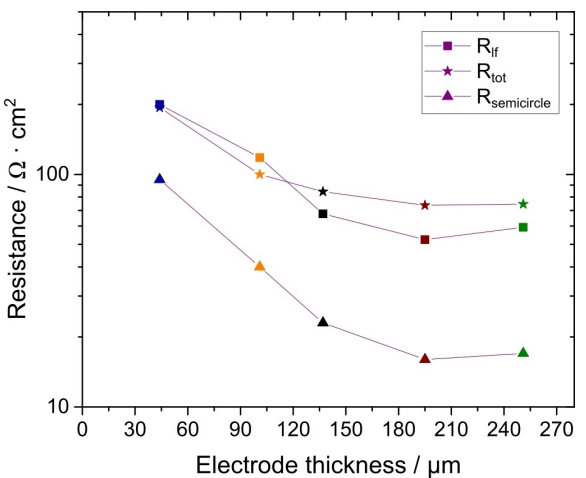


Figure 6. Dependence of the resistances R_{lf} , $R_{\text{semicircle}}$ and R_{tot} on electrode thickness. R_{tot} was obtained from the galvanostatic cycling curves shown in Figure 4, while R_{lf} and $R_{\text{semicircle}}$ were determined from the impedance spectra shown in Figure 5.

obtained for R_{lf} and R_{tot} are similar, while the values for $R_{\text{semicircle}}$ are considerably smaller. This is understandable, since both cycling at 0.1 C and impedance measurement at 10^{-4} Hz probe kinetic and transport limitations on long time scales in the range of 10^4 s. In contrast, $R_{\text{semicircle}}$ is determined by processes taking place on much shorter time scales. Consequently, the analysis of the thickness dependence of $R_{\text{semicircle}}$ is not sufficient for understanding the total resistance of the battery cells during cycling.

In order to analyze the thickness-dependent cathode impedance in more detail, we use a generalized transmission line model (GTLM) for the cathodes with cylindrical pores and high electronic conductivity.^[25] In this model, the total impedance of the cathode is given by:

$$Z^{\text{GTLM}} = \sqrt{\frac{Z_{\text{ion}} \cdot Z_{\text{loc}}}{I_p \cdot a_v}} \cdot \coth\left(\sqrt{\frac{Z_{\text{ion}} \cdot I_p \cdot a_v}{Z_{\text{loc}}}}\right) \quad (4)$$

With

$$Z_{\text{ion}} = \frac{I}{\sigma_{\text{ion}}^{\text{eff}}} + \left(\frac{I}{\sigma_{\text{ion}}^{\text{ABC,eff}}} - \frac{I}{\sigma_{\text{ion}}^{\text{eff}}} \right) \frac{\tanh(\Omega_{\text{ion}})}{\Omega_{\text{ion}}} \quad (5)$$

and

$$\Omega_{\text{ion}} = \sqrt{\frac{i\omega I_p^2}{D_{\text{salt}}}} \quad (6)$$

and

$$Z_{\text{loc}} = \left(\left(R_{\text{CT}} + \frac{dU}{dc_s} Y_s \right)^{-1} + i\omega C_{\text{DL}} \right)^{-1} \quad (7)$$

and

$$Y_s = \frac{R_{\text{ap}}}{FD_s} \cdot \frac{\tanh(\Omega_s)}{\tanh(\Omega_s) - \Omega_s} \quad (8)$$

and

$$\Omega_s = \sqrt{\frac{i\omega R_{\text{ap}}^2}{D_s}} \quad (9)$$

Z_{ion} denotes the impedance caused by ion transport in the electrolyte-filled pores, while Z_{loc} is the impedance related to double layer formation and charge transfer at the active material / electrolyte interface as well as to Li diffusion in the active material particles. $I_p = I \cdot \tau_{\text{EIS}}$ is the effective length of the electrolyte-filled pores, $a_v = \frac{3(1-\varepsilon_e)}{R_{\text{ap}}}$ is the surface of the active material particles per unit volume of the electrode, $\sigma_{\text{ion}}^{\text{eff}} = \frac{\sigma_{\text{ion}} \varepsilon_e}{\tau_{\text{EIS}}}$ is the effective ionic conductivity of the composite electrode without salt concentration polarization, $\sigma_{\text{ion},\text{eff}}^{\text{ABC}} = t_{\text{Li}^+}^{\text{ABC}} \cdot \sigma_{\text{ion}}^{\text{eff}}$, is the effective Li^+ ion conductivity of the composite electrode after concentration polarization, with $t_{\text{Li}^+}^{\text{ABC}} = \frac{1}{1 + \frac{2RT\sigma_{\text{ion}}}{F^2 D_{\text{salt}} c_{\text{salt}}} \frac{d\ln(a_v)}{d\ln(c_{\text{salt}})} \cdot (1-t_{\ell_s}^{\prime\prime})^2}$ denoting the Li^+ transference number under anion blocking conditions. $R_{\text{CT}} = \frac{RT}{Fj_0}$ and C_{DL} denote the area-specific charge transfer resistance and double layer capacitance, respectively, at the electrode / active material particle interface.

The model takes into account ion migration in the electrolyte-filled pores, formation of salt concentration gradients in these pores, double layer formation and charge transfer at the electrolyte/active material particle interface as well as Li chemical diffusion in the active material particles.

Most of the parameters in Equations (3–8) are known and are given in Table 1. Three parameters were taken as adjustable parameters, namely the dependence of the equilibrium electrode potential on the Li concentration, dU/dc_s at SOC50, the chemical diffusion coefficient of Li in the active material particles, D_s , and the exchange current density j_0 . The best agreement between experimental impedance spectra and the GTLM impedance spectra was obtained with $\frac{dU}{dc_s} = -5.5 \times 10^{-5} \text{ V m}^3 \text{ mol}^{-1}$, $D_s = 10^{-15} \text{ m}^2 \text{ s}^{-1}$ and $j_0 = 0.05 \text{ A m}^{-2}$, see Figure 7 and Table 1.

We note that in the literature, alternative TLM-type models can be found,^[35,36] which predict more than one semicircle in the impedance Nyquist plot. For instance, the impedance of

Table 1. Parameters used for calculating the cathode impedance in the framework of the generalized transmission line model (GTLM).

Parameter	Physical meaning	Value
σ_{ion}	Ionic conductivity	1 S m^{-1} ^[33]
D_{salt}	Salt diffusion coefficient	$3 \times 10^{-10} \text{ m}^2 \text{ s}^{-1}$ ^[33]
$\frac{d\ln(a_v)}{d\ln(c_{\text{salt}})}$	Thermodynamic factor	$2^{[34]}$
$t_{\text{Li}^+}^{\prime\prime}$	Mobility-based Li^+ transference number of the electrolyte	0.35
c_{salt}	Salt concentration	1000 mol m^{-3}
j_0	Exchange current density for cathode active material particles	0.05 A m^{-2}
T	Temperature	303.15 K
R_{ap}	Radius of the active material particles	$5.0 \times 10^{-6} \text{ m}$
ρ_{ap}	Active material mass density	5060 kg m^{-3}
ε_e	Volume fraction of electrolyte	0.35
τ_{EIS}	Ionic tortuosity	3.0
dU/dc_s	Dependence of electrode potential on Li concentration in the active material particles	$-5.5 \times 10^{-5} \text{ V m}^3 \text{ mol}^{-1}$
C_{DL}	double layer capacitance	$5 \times 10^{-2} \text{ F m}^{-2}$
D_s	Li chemical diffusion coefficient in active material particle	$1 \times 10^{-15} \text{ m}^2 \text{ s}^{-1}$

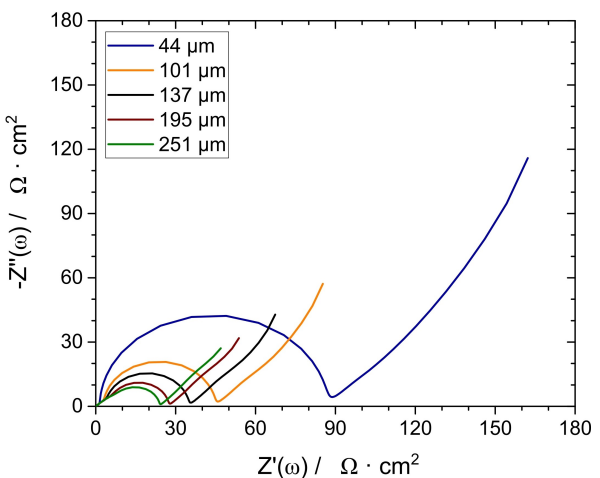


Figure 7. Simulation of the thickness-dependent cathode impedance spectra in the framework of a generalized transmission line model (GTLM) with parameters listed in Table 1.

the current collector / active material interface can lead to a high-frequency semicircle, and the ion transport inside the pore space and the charge transfer into the active material particles can lead to more than one semicircle. However, since we observe only a single semicircle and since the GTLM model spectra with a single set of parameters are in good agreement

with the experimental spectra, we conclude that the GTLM model is sufficient for describing the essential features of the thickness-dependent spectra.

Consequently, we used the GTLM results for estimating the thickness dependence of the overpotential during battery cycling at a high rate of 1 C. To this end, we first calculate the current density at 1 C, j_{1C} , which is proportional to the cathode thickness, see Supporting Information. The overpotential at 1 C is then approximated by $\eta_{1C} = R_{if}^{\text{GTLM}} \cdot j_{1C}$ with $R_{if}^{\text{GTLM}} = |Z^{\text{GTLM}}(10^{-4} \text{ Hz})|$. In Figure 8(a and d), R_{if}^{GTLM} and η_{1C} , respectively, are plotted versus cathode thickness. R_{if}^{GTLM} drops by a factor of about 4 when increasing the thickness from 44 \$\mu\text{m}\$ to 251 \$\mu\text{m}\$. The origin of this drop becomes clear when considering the modulus of the two impedances Z_{ion} and Z_{loc} at 10^{-4} Hz , $|Z_{\text{ion}}(10^{-4} \text{ Hz})|$ and $|Z_{\text{loc}}(10^{-4} \text{ Hz})|$, respectively, see Figure 8(a). In the limit of low electrode thicknesses, we have $|Z_{\text{loc}}(10^{-4} \text{ Hz})/(a_v \cdot I_p)| \gg |Z_{\text{ion}}(10^{-4} \text{ Hz})|$, and the GTLM predicts $Z^{\text{GTLM}}(10^{-4} \text{ Hz}) = Z_{\text{loc}}(10^{-4} \text{ Hz})/(a_v \cdot I_p)$ $+ \frac{1}{3} Z_{\text{ion}}(10^{-4} \text{ Hz}) \approx Z_{\text{loc}}(10^{-4} \text{ Hz})/(a_v \cdot I_p)$. $Z_{\text{loc}}(10^{-4} \text{ Hz})/(a_v \cdot I_p)$ drops with increasing thickness, since the interfacial area between active material particles and electrolyte increases. In the limit of high electrode thicknesses, we have $|Z_{\text{loc}}(10^{-4} \text{ Hz})/(a_v \cdot I_p)| \ll |Z_{\text{ion}}(10^{-4} \text{ Hz})|$, and the GTLM predicts $Z^{\text{GTLM}}(10^{-4} \text{ Hz}) = \sqrt{|Z_{\text{loc}}(10^{-4} \text{ Hz}) \cdot Z_{\text{ion}}(10^{-4} \text{ Hz})/(a_v \cdot I_p)}$, which is independent of thickness.

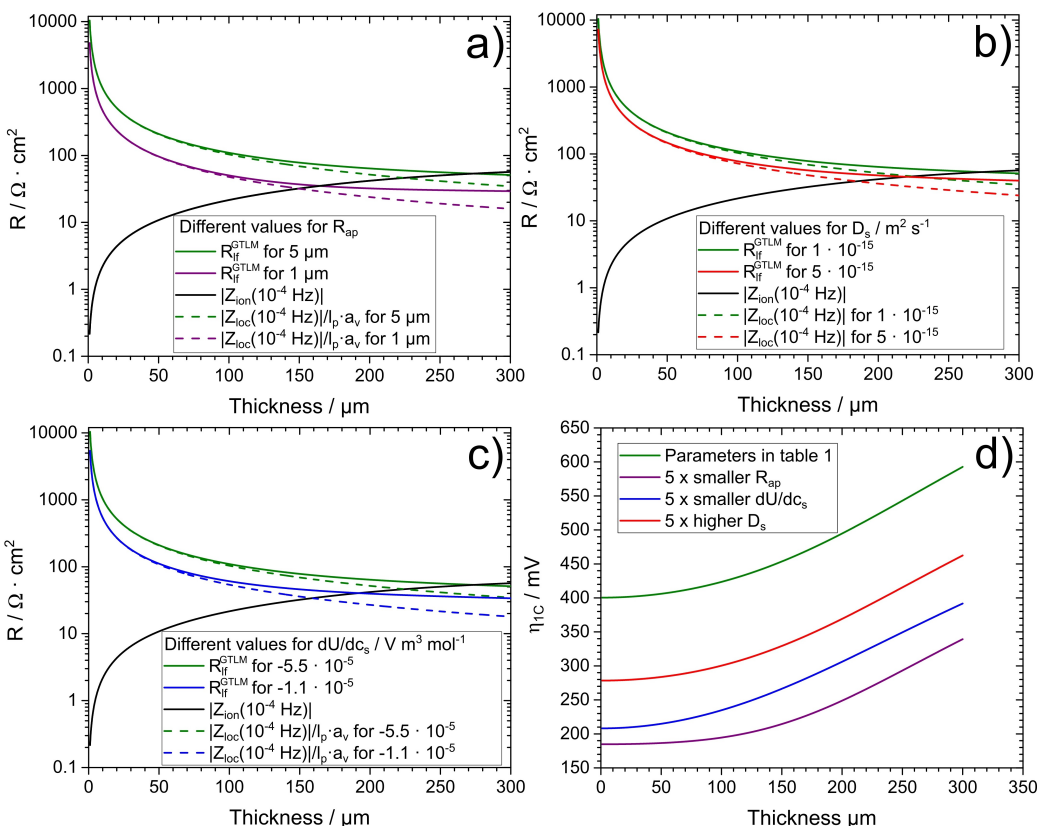


Figure 8. a-c) Thickness-dependent resistances R_{if}^{GTLM} , $|Z_{\text{ion}}(10^{-4} \text{ Hz})|$ and $\frac{|Z_{\text{loc}}(10^{-4} \text{ Hz})|}{I_p \cdot a_v}$ for two different active material radii R_{ap} , for two different Li diffusion coefficients in the active material particles D_s , and for two different dependences of electrode potential on Li concentration dU/dc_s , respectively. d) Thickness-dependent overpotential at a cycling rate of 1 C.

Although R_{lf}^{GTLM} decreases by a factor of about 4 when increasing the thickness from 44 μm to 251 μm , the increasing current density at 1 C leads to an increase of $\eta_{1\text{C}}$ by a factor of about 1.5, see green line in Figure 8(d). Therefore, the question arises in what way the overpotential for ultrathick electrodes can be reduced. The impedance caused by ion transport in the electrolyte-filled pores, Z_{ion} , is given by ion transport properties of the carbonate-based electrolyte, the volume fraction of the electrolyte-filled pores and by the tortuosity of the ion transport inside the pores. These parameters cannot be changed easily, since carbonate-based electrolytes are used in all commercial lithium-ion batteries, since the pore volume fraction cannot be increased without compromising the energy density and since a reduction of the ion transport tortuosity requires sophisticated techniques for optimizing the electrode morphology.^[13–16] The local impedance Z_{loc} , on the other hand, can be decreased by reducing the active material particle radius R_{ap} , and by using active material particles with higher Li diffusion coefficients D_s and lower $|dU/dc_s|$ values. In Figure 8(a–d), we illustrate the influence of a variation of these parameters by a factor of 5 on the low-frequency resistance R_{lf}^{GTLM} and the overpotential $\eta_{1\text{C}}$, respectively. As seen from Figure 8(d), a reduction of the active material particle radius from 5 μm to 1 μm reduces the overpotential $\eta_{1\text{C}}$ considerably, so that $\eta_{1\text{C}}$ for an ultrathick electrode with $l=300\text{ }\mu\text{m}$ and $R_{\text{ap}}=1\text{ }\mu\text{m}$ is lower than for a standard electrode with $l=80\text{--}100\text{ }\mu\text{m}$ and $R_{\text{ap}}=5\text{ }\mu\text{m}$. An increase of D_s by a factor of 5 and a reduction of $|dU/dc_s|$ by a factor of 5 exert a weaker influence on $\eta_{1\text{C}}$. These results give indication that a reduction of the active material particle size should be the most effective means for enabling cycling of ultrathick electrodes with a rate of 1 C. This can be achieved by using alternative preparation methods, such as hydrothermal syntheses.^[37–39] However, it is important to note that the particle size should not be too small, since degradation processes between nano-sized active material particles and electrolyte during battery cycling were found to be fast.^[37,38,40] Consequently, the optimum active material particle size should be around 1 μm or slightly below.

Conclusion

We have carried out a case study on the thickness-dependent impedance of LCO electrodes in a thickness range from 44 μm to 251 μm . The electrodes were prepared in a way that the tortuosity of the ion transport pathways was virtually independent of thickness. The impedance was found to decrease considerably with increasing thickness and to follow the predictions of a generalized transmission line model (GTLM). In addition, the total resistance during cycling of the electrodes R_{tot} was determined and compared to the impedance spectra. A good agreement was observed between R_{tot} and the low-frequency resistance $R_{lf}=|Z(10^{-4}\text{Hz})|$, while the resistance of the high-frequency semicircle $R_{\text{semicircle}}$ due to ion transport and charge transfer was considerably lower.

We have used the GTLM for analyzing the influence of three different parameters on the overpotential during fast cycling

with a rate of 1 C, namely the active material radius R_{ap} , the Li diffusion coefficient in the active material particles D_s , and the dependence of electrode potential on Li concentration, dU/dc_s . Our results show that a reduction of the active material particle radius to values in the range of 1 μm or slightly below should be the most effective means for enabling fast cycling of ultrathick electrodes.

Experimental Section

Electrode preparation

LiCoO_2 (LCO) composite electrodes with variable thickness were prepared from an *N*-Methyl-2-pyrrolidone-based (NMP 99.5%, Alfa Aesar, Thermo Fischer GmbH, Kandel, Germany) slurry of 90 wt% LCO (97.0%, Alfa Aesar), 5 wt% C-NERGY SUPER C65 carbon black (Timcal, Bodio, Switzerland) as conductivity additive, and 5 wt% polyvinylidene fluoride (PVDF, Solvay GmbH, Hannover). First, the binder was dissolved in NMP at 50 °C. Then the mixed LCO and carbon black powders were added to the solution in portions of 10 g and mixed at 20000 rpm by means of a T 25 disperser (IKA, Staufen, Germany) for three minutes (3 × 1 minute) each. The resulting slurry was casted onto an aluminum foil. The thickness of the films was adjusted using a ZAA 2300 automatic film applicator (Zehntner, Sissach, Switzerland). The foils were dried for 24 hours at 80 °C under air atmosphere and then transferred into an argon filled glovebox (Unilab, MBraun, Germany, $X_{\text{H}_2\text{O}}<1\text{ ppm}$, $X_{\text{O}_2}<1\text{ ppm}$). Subsequently, the films were compacted by using a hot rolling press heated at 80 °C (MSK-HRP-01, MTI Corporation, Richmond, USA). In order to achieve the desired porosity, the gap between the two heated rolls was reduced, and an electrode was punched out. The thickness and weight of each disc electrode excluding the current collector was determined in order to calculate the porosity. If the porosity of the electrode was still too high, the gap was lowered and the procedure was repeated, until the desired porosity was reached. Finally, discs with a diameter of 11.85 mm were cut out of the electrode films. To this end, the weight and thickness of 50 aluminum discs with the same diameter were measured, averaged, and subtracted from the measured weight and thickness of the electrodes.

Determination of the ion transport tortuosity

The ion transport tortuosities of the electrodes were determined in a symmetrical setup cathode | separator | cathode using a TSC battery cell (rhd instruments, Darmstadt, Germany). Two electrodes with the same thickness and volume fraction of electrolyte were separated by three Whatman separators and soaked with 120 μL electrolyte. The cells were equilibrated overnight, and impedance measurements were carried out in a frequency range from 10^5 to 10^{-1} Hz with an applied rms ac voltage of 10 mV. The spectra were fitted to a specific transmission-line model^[41] using the analysis software RelaxIS 3.0 (rhd instruments). This specific TLM takes into account the ion transport inside the electrolyte-filled pores and the double layer capacitance of the active material / electrolyte interfaces.

Galvanostatic cycling studies

Battery cells were assembled in an argon-filled glovebox (Unilab, MBraun, Germany, $X_{\text{H}_2\text{O}}<1\text{ ppm}$, $X_{\text{O}_2}<1\text{ ppm}$). Galvanostatic cycling was carried out in a three-electrode setup (TSC battery cell, rhd instruments, Darmstadt, Germany) with the composite cathode

acting as working electrode and with metallic lithium acting as counter and reference electrode. Cycling was performed at 30 °C between 4.3 V and 2.7 V as upper and lower cutoff potential using a Multi Autolab/M101 (Metrohm Autolab BV, Utrecht Netherlands).

Electrochemical impedance spectroscopy at SOC50

The electrochemical impedance measurements were carried out by means of a Multi Autolab/M101 equipped with a FRA32 M impedance modul (Metrohm Autolab BV, Utrecht, Netherlands) at 50% state of charge (SOC50). The charge was calculated from the maximum discharge capacity achieved in the third cycle. An AC voltage amplitude of 10 mV was applied, and the frequency range extended from 10⁵ Hz to 10⁻⁴ Hz. Impedance spectra were analyzed using the software RelaxIS3 (rhd instruments, Darmstadt, Germany).

Acknowledgements

Open Access funding enabled and organized by Projekt DEAL.

Conflict of Interest

The authors declare no conflict of interest.

Data Availability Statement

Research data are not shared.

Keywords: cathode impedance • lithium-ion batteries • thick electrodes • tortuosity • transmission line model

- [1] V. Etacheri, R. Marom, R. Elazari, G. Salitra, D. Aurbach, *Energy Environ. Sci.* **2011**, *4*, 3243.
- [2] S.-T. Myung, F. Maglia, K.-J. Park, C. S. Yoon, P. Lamp, S.-J. Kim, Y.-K. Sun, *ACS Energy Lett.* **2017**, *2*, 196–223.
- [3] M. Bianchini, M. Roca-Ayats, P. Hartmann, T. Brezesinski, J. Janek, *Angew. Chem. Int. Ed.* **2019**, *58*, 10434–10458; *Angew. Chem.* **2019**, *131*, 10542–10569.
- [4] J. Kim, H. Lee, H. Cha, M. Yoon, M. Park, J. Cho, *Adv. Energy Mater.* **2018**, *8*, 1702028.
- [5] H.-J. Noh, S. Youn, C. S. Yoon, Y.-K. Sun, *J. Power Sources* **2013**, *233*, 121–130.
- [6] H.-H. Sun, W. Choi, J. K. Lee, I.-H. Oh, H.-G. Jung, *J. Power Sources* **2015**, *275*, 877–883.
- [7] C. H. Chen, J. Liu, M. E. Stoll, G. Henriksen, D. R. Vissers, K. Amine, *J. Power Sources* **2004**, *128*, 278–285.
- [8] S. Chae, S.-H. Choi, N. Kim, J. Sung, J. Cho, *Angew. Chem. Int. Ed.* **2020**, *59*, 110–135; *Angew. Chem.* **2020**, *132*, 112–138.
- [9] C.-H. Doh, C.-W. Park, H.-M. Shin, D.-H. Kim, Y.-D. Chung, S.-I. Moon, B.-S. Jin, H.-S. Kim, A. Veluchamy, *J. Power Sources* **2008**, *179*, 367–370.
- [10] Y. Kobayashi, S. Seki, Y. Mita, Y. Ohno, H. Miyashiro, P. Charest, A. Guerfi, K. Zaghib, *J. Power Sources* **2008**, *185*, 542–548.
- [11] A. Franco Gonzalez, N.-H. Yang, R.-S. Liu, *J. Phys. Chem. C* **2017**, *121*, 27775–27787.
- [12] Y. Kuang, C. Chen, D. Kirsch, L. Hu, *Adv. Energy Mater.* **2019**, *9*, 1901457.
- [13] Z. Zhao, M. Sun, W. Chen, Y. Liu, L. Zhang, N. Dongfang, Y. Ruan, J. Zhang, P. Wang, L. Dong, Y. Xia, H. Lu, *Adv. Funct. Mater.* **2019**, *29*, 1809196.
- [14] J. Park, C. Jeon, W. Kim, S.-J. Bong, S. Jeong, H.-J. Kim, *J. Power Sources* **2021**, *482*, 228948.
- [15] C. Huang, N. P. Young, J. Zhang, H. J. Snaith, P. S. Grant, *Nano Energy* **2017**, *31*, 377–385.
- [16] J. Park, S. Hyeon, S. Jeong, H.-J. Kim, *J. Ind. Eng. Chem.* **2019**, *70*, 178–185.
- [17] L. S. Kremer, A. Hoffmann, T. Danner, S. Hein, B. Prifling, D. Westhoff, C. Dreer, A. Latz, V. Schmidt, M. Wohlfahrt-Mehrens, *Energy Technol.* **2020**, *8*, 1900167.
- [18] Z. Du, D. L. Wood, C. Daniel, S. Kalnaus, J. Li, *J. Appl. Electrochem.* **2017**, *47*, 405–415.
- [19] R. Zhao, J. Liu, J. Gu, *Appl. Energy* **2015**, *139*, 220–229.
- [20] M. Singh, J. Kaiser, H. Hahn, *J. Electrochem. Soc.* **2015**, *162*, A1196–A1201.
- [21] M. Singh, J. Kaiser, H. Hahn, *J. Electroanal. Chem.* **2016**, *782*, 245–249.
- [22] X. Wu, S. Xia, Y. Huang, X. Hu, B. Yuan, S. Chen, Y. Yu, W. Liu, *Adv. Funct. Mater.* **2019**, *29*, 1903961.
- [23] H. Gao, Q. Wu, Y. Hu, J. P. Zheng, K. Amine, Z. Chen, *J. Phys. Chem. Lett.* **2018**, *9*, 5100–5104.
- [24] J. Landesfeind, J. Hattendorff, A. Ehrl, W. A. Wall, H. A. Gasteiger, *J. Electrochem. Soc.* **2016**, *163*, A1373–A1387.
- [25] M. Cronau, M. Kroll, M. Szabo, F. Sälzer, B. Roling, *Batteries & Supercaps* **2020**, *3*, 611–618.
- [26] M. Kroll, S. L. Karstens, M. Cronau, A. Höltzel, S. Schlabach, N. Nobel, C. Redenbach, B. Roling, U. Tallarek, *Batteries & Supercaps* **2021**, *4*, 1363–1373.
- [27] T.-T. Nguyen, A. Demortière, B. Fleutot, B. Delobel, C. Delacourt, S. J. Cooper, *NPJ Comput. Mater.* **2020**, *6*, 123.
- [28] A. Shodiev, E. N. Primo, M. Chouchane, T. Lombardo, A. C. Ngandjong, A. Rucci, A. A. Franco, *J. Power Sources* **2020**, *454*, 227871.
- [29] J. Landesfeind, M. Ebner, A. Eldiven, V. Wood, H. A. Gasteiger, *J. Electrochem. Soc.* **2018**, *165*, A469–A476.
- [30] M. Singh, J. Kaiser, H. Hahn, *Batteries* **2016**, *2*, 35.
- [31] L. Wang, B. Chen, J. Ma, G. Cui, L. Chen, *Chem. Soc. Rev.* **2018**, *47*, 6505–6602.
- [32] Q. Liu, X. Su, D. Lei, Y. Qin, J. Wen, F. Guo, Y. A. Wu, Y. Rong, R. Kou, X. Xiao, F. Aguesse, J. Bareño, Y. Ren, W. Lu, Y. Li, *Nat. Energy* **2018**, *3*, 936–943.
- [33] L. O. Valegen, J. N. Reimers, *J. Electrochem. Soc.* **2005**, *152*, A882.
- [34] A. Nyman, M. Behm, G. Lindbergh, *Electrochim. Acta* **2008**, *53*, 6356–6365.
- [35] J. Moškon, J. Žuntar, S. Drvarić Talian, R. Dominko, M. Gaberšček, *J. Electrochem. Soc.* **2020**, *167*, 140539.
- [36] M. Gaberšček, *Nat. Commun.* **2021**, *12*, 6513.
- [37] M. Jo, Y.-S. Hong, Choo Jaebum, J. Cho, *J. Electroanal. Chem.* **2009**, *156*, A430–A434.
- [38] M. Okubo, E. Hosono, J. Kim, M. Enomoto, N. Kojima, T. Kudo, H. Zhou, I. Honma, *J. Am. Chem. Soc.* **2007**, *129*, 7444–7452.
- [39] T. Kawamura, M. Makidera, S. Okada, K. Koga, N. Miura, J. Yamaki, *J. Power Sources* **2005**, *146*, 27–32.
- [40] H. Liu, J. Wang, X. Zhang, D. Zhou, X. Qi, B. Qiu, J. Fang, R. Kloepsch, G. Schumacher, Z. Liu, J. Li, *ACS Appl. Mater. Interfaces* **2016**, *8*, 4661–4675.
- [41] N. Ogihara, S. Kawauchi, C. Okuda, Y. Itou, Y. Takeuchi, Y. Ukyo, *J. Electrochem. Soc.* **2012**, *159*, A1034–A1039.

Manuscript received: April 26, 2022

Revised manuscript received: June 13, 2022

Version of record online: July 4, 2022